

# Accelerated Band Offset Prediction in Semiconductor Interfaces with DFT and Deep Learning

Kamal Choudhary<sup>1,\*</sup> and Kevin F. Garrity<sup>2</sup>

<sup>1</sup>Material Measurement Laboratory, National Institute of Standards and Technology, Maryland, 20899, USA.

\*Electronic mail: [kamal.choudhary@nist.gov](mailto:kamal.choudhary@nist.gov)

## ABSTRACT

We introduce a computational framework to predict band offsets of semiconductor interfaces using density functional theory (DFT) and graph neural networks (GNN). As a first step, we benchmark DFT based work function and electron affinity values for surfaces against experimental data with accuracies of 0.29 eV and 0.39 eV. Similarly, we evaluate band offset values using independent unit (IU) and alternate slab junction (ASJ) models leading to accuracies of 0.45 eV and 0.22 eV respectively. During ASJ structure generation, we use Zur's algorithm along with a unified GNN force-field to tackle the conformation challenges of interface design. At present, we have 300 surface work functions calculated with DFT, from which we can compute 44850 IU band offsets as well as 250 directly calculated ASJ band offsets. Finally, as the space of all possible heterojunctions is too large to simulate with DFT, we develop generalized GNN models to quickly predict band edges with an accuracy of 0.26 eV. We use such models to predict relevant quantities including ionization potentials, electron affinities, and IU-based band offsets. We establish simple rules using the above models to pre-screen potential semiconductor devices from a vast pool of nearly 1.4 trillion candidate interfaces.

## Introduction

Interfaces are critical for a variety of technological applications including semiconductor transistors and diodes, solid-state lighting devices, solar-cells, data-storage and battery applications<sup>1-6</sup>. While interfaces are ubiquitous, predicting even basic interface properties from bulk data or chemical models remains challenging. Furthermore, the continued scaling of devices towards the atomic limit<sup>7</sup> makes interface properties even more important. There have been numerous scientific efforts to model interfaces with a variety of techniques including density functional theory (DFT)<sup>8-17</sup>, force-field<sup>18-21</sup>, tight-binding<sup>22-25</sup> and machine learning techniques<sup>16,26-28</sup>. However, to the best of our knowledge, there is no systematic investigation of interfaces for a large class of structural variety and chemical compositions. Most of the previous efforts focus on a limited number of interfaces, and hence there is a need for a dedicated infrastructure for data-driven interface materials design.

Some of the key quantities for determining interface properties are: equilibrium geometries, energetics, work functions, ionization potentials, electron affinities, band offsets, carrier effective masses, mobilities, and thermal conductivities. Calculations of band offsets and band-alignment at semiconductor heterojunctions are of special interest for device design. Semiconductor device transport and performance depend critically on valence band offsets ( $\Delta E_v$ ) and conduction band offsets ( $\Delta E_c$ ), as well as interfacial roughness and defects<sup>29-31</sup>. Based on the band-alignment, heterostructures can be categorized into three classes: (i) type-I (straddling gap), (ii) type-II (staggered gap), and (iii) type-III (broken gap). The type-I heterostructures are used for transistors, lasers and light-emitting diode (LED) applications, type-II are used for photoabsorbers and photocatalysts, and type-III are used for tunneling field effect transistors.

Experimentally, band offsets can be measured using optical spectroscopy, X-ray photoelectron spectroscopy (XPS), ultraviolet photoelectron spectroscopy (UPS), and electrical measurements<sup>3</sup>. However, these experiments can be quite time and resource consuming. Additionally, the variability across multiple reported measurements can be reasonably high. For example, the reported AlN/GaN interface  $\Delta E_v$  varies from 0.57 eV to 1.36 eV with reported uncertainties of up to 0.24 eV<sup>31</sup>. In this respect, the computation of band offsets can serve as a complementary tool to experimental analysis. Nevertheless, the calculation of band offsets is rather challenging<sup>32</sup> and has been an area of research for about a century<sup>33-35</sup>. Density functional theory calculations are one of the most widely used techniques for predicting band offsets, as they can describe the electronic and atomic structure at the interface in a self-consistent manner. There are two main approaches to predicting band offsets using DFT. The first is to directly simulate the interface using either an alternating slab-junction (ASJ)/superlattice or surface terminated junction (STJ)/slab vacuum geometry, either of which requires a computationally expensive calculation for each pair of materials. Alternatively, the independent unit (IU)/electron affinity/Anderson's model<sup>13,36</sup> requires only independent surface calculations of each material, greatly reducing computational cost but ignoring specific interface effects. ASJ models were

shown to be most accurate in Ref.<sup>13</sup>, but IU models are surprisingly competitive.

Importantly, the generation of an atomistic interface geometry is a challenging task due to the high number of possible conformations and configurations. There are several important factors determining an interface such as: the selection of the lattice alignment, the relative orientation/displacement between surfaces, the separation distance, point/line defects, and the presence of interfacial charge transfer. Several previous tools have attempted to address this challenge, including MPIInterfaces<sup>15</sup>, TribChem<sup>37</sup> and QuantumATK<sup>38</sup> packages.

Moreover, DFT calculations of interfaces require initial pre-relaxed bulk structures which in this work are obtained from the Joint Automated Repository for Various Integrated Simulations (JARVIS)-DFT<sup>39,40</sup> database containing nearly 80000 bulk 3D and 1100 2D materials. The JARVIS-DFT originated about 5 years ago and contains millions of properties materials and has carefully converged atomic structures with tight convergence parameters, various exchange-correlation functionals such as OptB88vdW<sup>41</sup>, TBmBJ<sup>42</sup>, R2SCAN<sup>43</sup> and HSE06<sup>44</sup>. JARVIS-DFT contains metallic, semiconducting, insulator, superconductor, high-strength, topological, solar, thermoelectric, piezoelectric, dielectric, two-dimensional, magnetic, porous, defect and various other classes of bulk materials<sup>45,46</sup>. We have also previously looked at the band alignment of layered two dimensional materials using JARVIS-DFT<sup>16</sup>. However, three dimensional systems with chemical bonding between the materials require much greater effort, as the interfacial bonding has a much greater effect of the interface properties, and the determination of even a single interface structure is a challenging task. Out of above material class combinations, semiconductor-semiconductor are of special interest for this work. As DFT calculations can be time-consuming for surfaces and interfaces machine-learning (ML)/deep learning (DL) techniques based on DFT data can be used to accelerate atomistic predictions<sup>47,48</sup>. Such models have often been applied for bulk property predictions and their applicability for defects and interfaces remains an open question. Several machine learning tools available in JARVIS such as classical force-field inspired descriptors (CFID)<sup>40</sup>, atomistic line graph neural network (ALIGNN)<sup>49</sup>, computer vision for atomistic images (AtomVision)<sup>50</sup> and natural language processing for chemistry (ChemNLP)<sup>51</sup> can be used in this regards to accelerate the interface design tasks. In particular, ALIGNN has been used to develop several fast surrogate models for property predictions as well as a unified force-field for fast structure optimizations.

Most importantly, for all the above predictions, it is important to benchmark and quantify error with respect to experimental data to gain confidence in predictions. This work addresses the above challenges and provides a streamlined framework for semiconductor interface design (InterMat). Although focusing on semiconductors, this work has relevance to other applications such as battery, data-storage, and solar-cell devices. We believe that this work will be a precursor to more thorough theoretical and experimental investigations of semiconductor interfaces.

## Results and discussion

A schematic overview of the combinatorial problem of interfaces and our approach is shown in Fig. 1. Initial atomic structures are obtained from the JARVIS-DFT repository. Out of 80000 materials available in JARVIS-DFT, we select 20901 semiconductors with OptB88vdW bandgap thresholds from 0.1 eV and 6 eV. Using a maximum Miller index (M) of 1, 2, and 3, the number of symmetrically distinct surface slabs are 186847, 591639 and 1642584, respectively. Using these surfaces, the number of binary interface systems that can be generated are 17.5 billion, 175 billion and 1.4 trillion. Including different surface terminations and defects at the interfaces can lead to further possible combinations. It is unrealistic to analyze such a large search space to find combinations for devices by using conventional experimental or computational techniques. We will instead use the ALIGNN models to guide and prioritize DFT calculations among the vast pool of candidates. We develop machine learning models for fast predictions of valence band maxima (VBM) and conduction band minima (CBM) using ALIGNN. These predictions can be further used for fast IU based band alignment using electron affinity/Anderson's rule<sup>36</sup>. To assess the strengths and limitations of such models, we develop a surface dataset for IU models and an interface datasets for ASJ models using DFT. We particularly focus on industrially relevant semiconductors including group IV (C, Si, Ge etc.), III-IV (AlN, GaN, GaAs, GaP, InSb etc.), II-VI (CdS, CdSe, ZnO, ZnS etc.). We also assess the strengths and limitations of IU and ASJ models against experimental measurements. The DFT dataset hence generated for surfaces and interfaces can then be fed back to fine tune the ALIGNN models to further improve accuracy.

### DFT dataset of work function, electron affinity, ionization potential and surface energy

We develop a dataset of non-polar unreconstructed slab surfaces using the JARVIS-DFT workflow. We carefully benchmark work function ( $\phi$ ), electron affinity ( $\chi$ ) and surface energy ( $\gamma$ ) values against experimental measurements from the literature. Recently, it was shown that vacuum and slab thicknesses of at least 10 Å are sufficient for surface models<sup>72</sup>. Usually, both of these parameters should be converged for each surface, but here for computational cost reasons, we use a fixed value for the thickness and vacuum padding. We use a 1.6 nm thickness and 1.2 nm vacuum in this work. During the DFT calculations, the converged K-point<sup>73</sup> values from the relevant bulk calculations are used for surfaces also. We optimize the internal coordinates of these surfaces keeping the cell volume constant. We obtain the OptB88vdW VBM and vacuum level (from the maximum

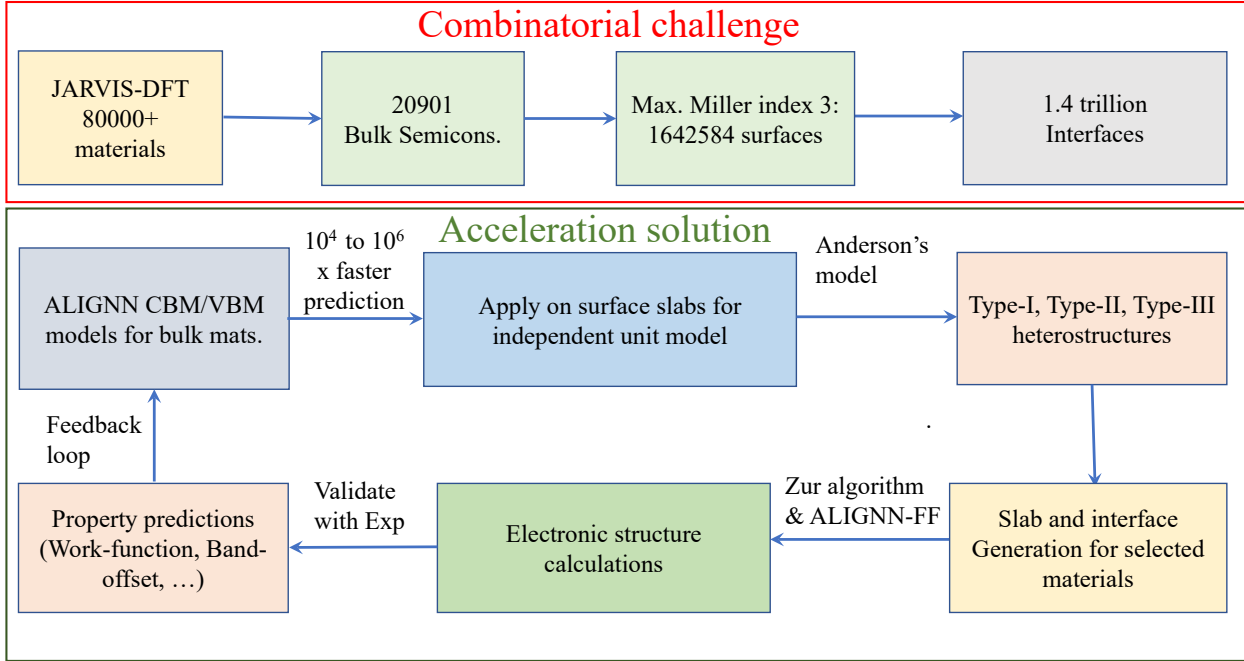


**Figure 1.** Schematic overview of the workflow. The number of possible semiconductor-semiconductor interfaces is exceedingly large. The workflow aims to provide a toolkit to generate interface structures and use multi-fidelity methods to accelerate interface/heterostructure design.

value of average electrostatic potential) of surface slabs using DFT. Subtracting the vacuum level from the VBM provides ionization potential (IP) information. Then, we add the bandgap ( $E_g$ ) of the material to the ionization potential to get the electron affinity (EA,  $\chi$ ). In order to benchmark our surface dataset, we compare work functions of these surfaces in Table 1 which shows excellent agreement with experiments with a mean absolute error value of 0.29 eV, consistent with previous benchmarking efforts. Similarly, we obtain a mean absolute error of 0.39 eV and  $0.34 \text{ Jm}^{-2}$  for electron affinity and surface energy data respectively. Currently, there are 300 surface data calculated using the workflow and the dataset is still growing. Using, these 300 surfaces, 44850 IU-band offsets can be predicted. Also, we plan to include reconstructed and polar surfaces in the future.

### ALIGNN models for bulk and surface band edges

We seek to accelerate the prediction of band edges using ML models, but the absolute prediction of band edges relative to vacuum requires DFT calculations with surfaces, which significantly limits our potential dataset. The JARVIS-DFT dataset contains a much larger dataset of three dimensional materials with CBM and VBM values using the VASP convention that the average electrostatic potential of a unit cell is set to zero. We first train an ML model using ALIGNN based on these bulk quantities, and then below we will show that the model is useful for predictions of relative work function and band edges.

In ALIGNN, a crystal structure is represented as a graph using atomic elements as nodes and atomic bonds as edges. Each node in the atomistic graph is assigned 9 input node features based on its atomic species: electronegativity, group number, covalent radius, valence electrons, first ionization energy, electron affinity, block and atomic volume. The inter-atomic bond distances are used as edge features with radial basis function up to  $8 \text{ \AA}$  cut-off and a 12-nearest-neighbor ( $N$ ). This atomistic graph is then used for constructing the corresponding line graph using interatomic bond-distances as nodes and bond-angles as edge features. ALIGNN uses edge-gated graph convolution for updating nodes as well as edge features using a propagation function ( $f$ ) for layer ( $l$ ), atom features ( $h$ ), and node ( $i$ ), details of which can be found in Ref.<sup>49,74</sup>:

$$h_i^{(l+1)} = f(h_i^l \{h_j^l\}_i) \quad (1)$$

We split each dataset into 90:5:5 train:validation:test parts. We train on 90 % train data and evaluate the validation and test data using ALIGNN. We find a mean absolute error (MAE) of 0.28 eV for CBM and VBM while the data can vary from -10 to

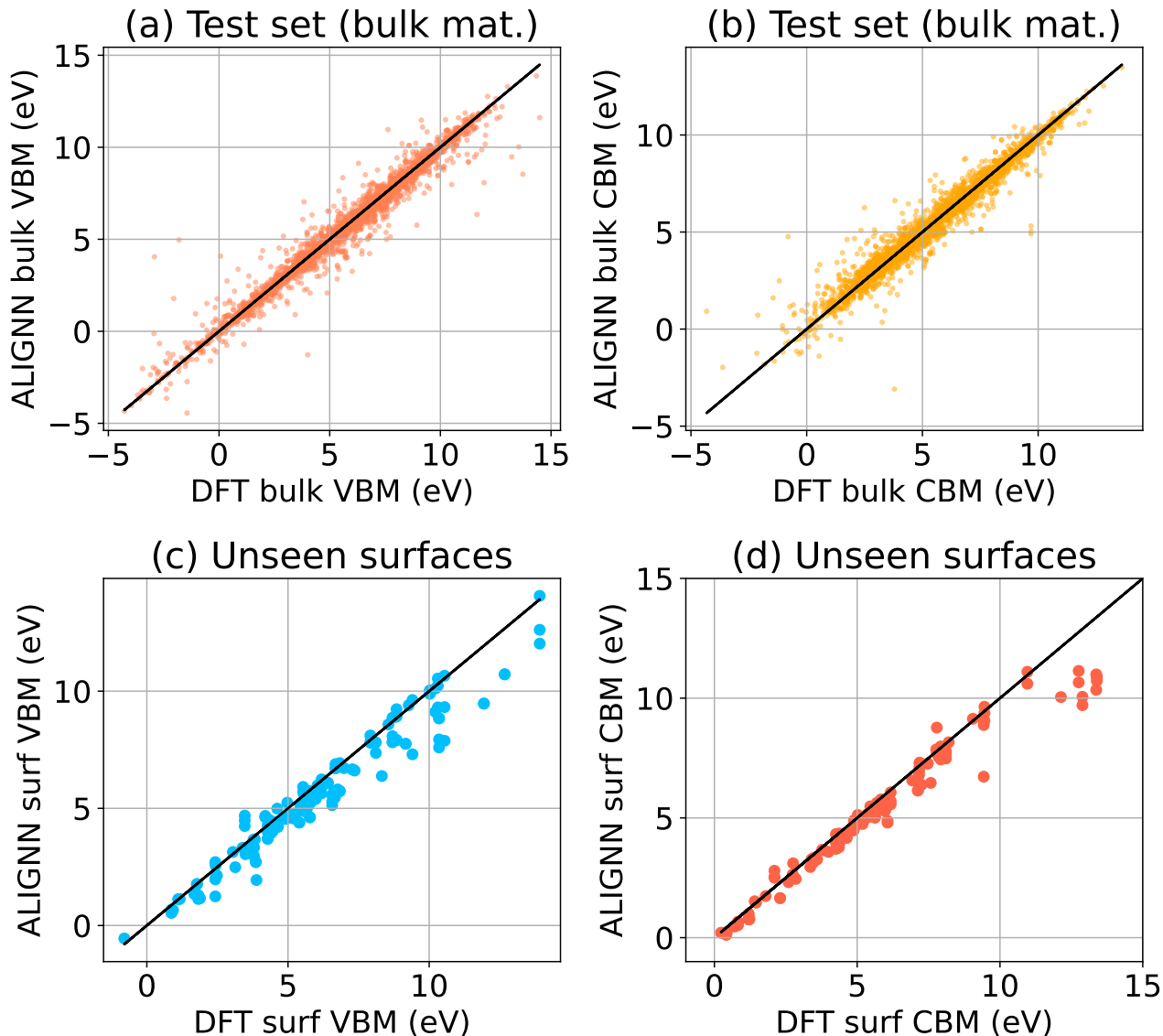


**Figure 2.** ALIGNN based regression models for a) VBM for JARVIS-DFT 3D/bulk materials test set data, b) CBM for bulk materials test set data, c) slab surface VBMs not part of the training set to evaluate extrapolation strength, d) slab surface CBMs not part of the training set to evaluate extrapolation strength.

10 eV suggesting that the model should be reasonable for predictions. The mean absolute deviation (MAD) for the CBM and VBM are 2.08 eV and 2.67 eV, respectively, so the MAD:MAE is nearly 10 relative to a trivial baseline model. Out of several other material properties trained using ALIGNN<sup>49</sup>, CBM/VBM models has one of the higher MAD:MAE ratios, especially compared to other electronic properties like the band gap. We show the CBM and VBM prediction models in Fig.2a and Fig.2b respectively. We believe with more data using the active learning loop we can further increase the MAD:MAE in future<sup>47</sup>.

Next, we evaluate the bulk-trained ALIGNN models on the DFT surface dataset and show results in Fig.2c and Fig.2d for CBM and VBM respectively. Interestingly, most of the data points are on  $x = y$  line suggesting excellent agreement. We find MAE values of 0.55 eV and 0.96 eV for VBM and CBM respectively. It is interesting to note that the error in CBM is higher than that of VBM, perhaps an explanation why predicting bandgaps of materials using machine learning is ever-standing difficult problem. We only use the VBM predicted from the ALIGNN model for the slab and add the bandgap value of the bulk material from JARVIS-DFT to get the CBM. Note the AI model was not trained on any surface structures suggesting that our models have high extrapolation power. Similar successful extrapolations for bulk-trained models were observed in Ref.<sup>75</sup> for

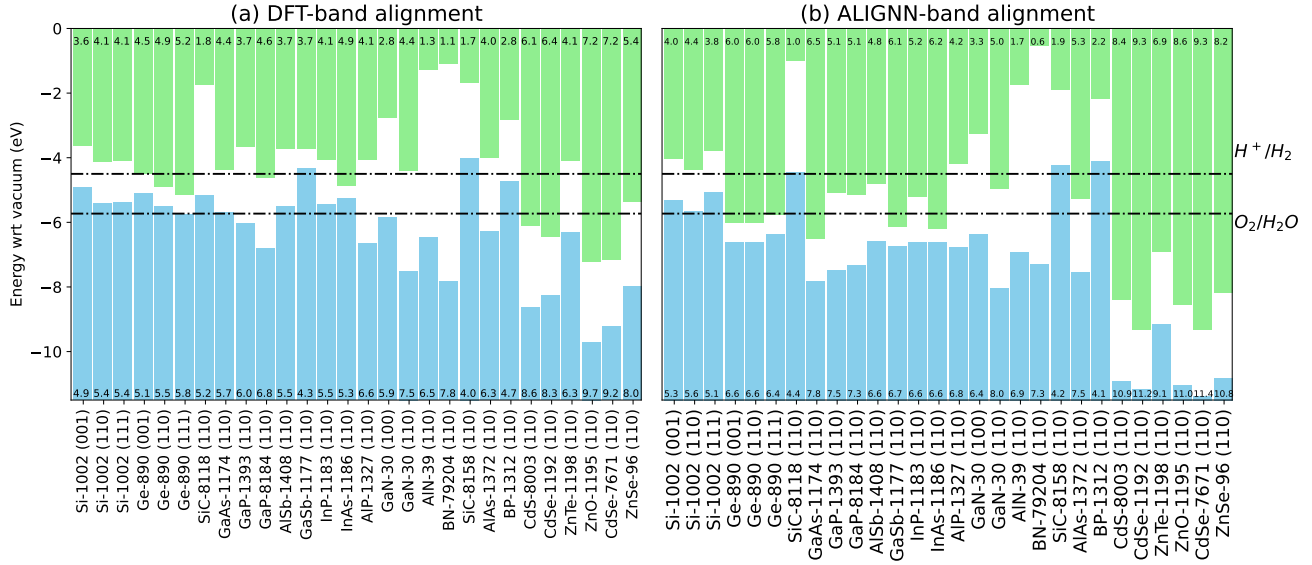


**Figure 3.** A few examples of band alignment based on the ionization potential (IP) and electron affinity (EA) for Anderson’s/independent unit (IU) model. a) Density functional theory based alignments can be used to obtain band offsets. b) Fast ALIGNN based band alignment predictions. The numbers in the green bars represent electron affinity while that in the blue bars represent ionization potentials. The trained models based band alignment will be available at JARVIS-Heterostructure website soon.

vacancies.

In order to translate the results from the ALIGNN model to absolute band energies relative to vacuum, we need access to the vacuum levels. Interestingly, we find that for the fixed slab and vacuum thicknesses used in this work, the vacuum levels are clustered around 5 eV even across different material chemistries. Because the vacuum values are reasonably constant, it is possible to predict relative band alignments using the ALIGNN model. Relative band alignments are more important than absolute values for classification into the three heterostructure types.

### DFT and ALIGNN based IU band alignment

IU band alignment, also known as Anderson’s rule<sup>36</sup>, predicts semiconductor band offsets at interfaces using only the IP and EA data from independent surface calculations. For a semiconductor heterojunction between A and B, the conduction band offset can be given by:

$$\Delta E_c = \chi_B - \chi_A \quad (2)$$

Similarly, the valence band offset is given by:

$$\Delta E_v = (\chi_A + E_{gA}) - (\chi_B + E_{gB}) \quad (3)$$

In Fig.3a, we show the DFT-based IU band alignments for a set of well-known semiconductor surfaces. We also include dotted lines for the energy levels of H<sub>2</sub> and H<sub>2</sub>O, which are relevant for photo-catalyst applications. We compare the DFT based IU band offsets for 8 interfaces in Table 2 against experiments. We find a mean absolute error of 0.45 eV which is similar to a value of 0.32 eV as found in ref.<sup>13</sup> for different systems.

We visualize IU based band alignment using ALIGNN model in Fig. 3b. We observe that the overall trends of DFT and ALIGNN closely resemble each other. For these surfaces, we calculate the classification accuracy of the heterostructures in type-I, type-II and type-III heterostructures. We find precision scores of 66.7 %, 66.1 % and 58.2 % respectively. Precision is defined as the fraction of relevant instances among all of the retrieved instances. The classification precision scores are based on DFT optimized surfaces, which are not available for all the materials in the database. So, we generate structures directly from the bulk counterparts, relax them using ALIGNN-FF and then predict the electron affinity and ionization potentials using the

**Table 1.** Work function ( $\phi$ , eV), electron affinity ( $\chi$ , eV) and surface energy ( $\gamma$ ,  $Jm^{-2}$ ) of a few unreconstructed non-polar surface slabs from OptB88vdW (OPT) against experimental data. The IDs represent JARVIS-DFT identifiers.

System	IDs	Miller	$\phi$ (OPT)	$\phi$ (Exp)	$\chi$ (OPT)	$\chi$ (Exp)	$\gamma$ (OPT)	$\gamma$ (Exp)
Si	1002	111	5.00	4.77 <sup>52</sup>	4.10	4.05 <sup>53</sup>	1.60	1.14 <sup>54</sup>
Si	1002	110	5.30	4.89 <sup>52</sup>	4.10	-	1.66	1.9 <sup>54</sup>
Si	1002	001	5.64	4.92 <sup>52</sup>	3.60	-	2.22	2.13 <sup>55</sup>
C	91	111	4.67	5.0 <sup>56</sup>	-2.9	-	5.27	5.50 <sup>57</sup>
Ge	890	111	4.87	4.80 <sup>58</sup>	5.2	4.13 <sup>29</sup>	0.99	1.30 <sup>55</sup>
SiGe	105410	111	4.93	4.08 <sup>59</sup>	4.5	-	1.36	-
SiC	8118	001	5.26	4.85 <sup>60</sup>	1.3	-	3.51	-
GaAs	1174	110	4.89	4.71 <sup>61</sup>	4.40	4.07 <sup>53</sup>	0.67	0.86 <sup>54</sup>
InAs	1186	110	4.85	4.90 <sup>61</sup>	4.9	4.9 <sup>29</sup>	0.57	-
AlSb	1408	110	5.11	4.86 <sup>61</sup>	3.70	3.65 <sup>29</sup>	0.77	-
GaSb	1177	110	4.48	4.76 <sup>61</sup>	3.70	4.06 <sup>29</sup>	0.71	-
AlN	39	100	5.56	5.35 <sup>60</sup>	1.3	2.1 <sup>62</sup>	2.27	-
GaN	30	100	5.74	5.90 <sup>63</sup>	2.8	3.3 <sup>64</sup>	1.67	-
BN	79204	110	6.84	7.0 <sup>65</sup>	1.4	-	2.41	-
GaP	1393	110	5.31	6.0 <sup>60</sup>	4.0	4.3 <sup>53</sup>	0.88	1.9 <sup>54</sup>
BP	1312	110	5.61	5.05 <sup>66</sup>	2.8	-	2.08	-
InP	1183	110	5.17	4.65 <sup>61</sup>	4.10	4.35 <sup>53</sup>	0.73	-
CdSe	1192	110	5.70	5.35 <sup>67</sup>	6.4	-	0.38	-
ZnSe	96	110	5.67	6.00 <sup>68</sup>	5.4	-	0.44	-
ZnTe	1198	110	5.17	5.30 <sup>69</sup>	4.10	3.5 <sup>29</sup>	0.36	-
Al	816	111	4.36	4.26 <sup>56</sup>	-	-	0.82	-
Au	825	111	5.5	5.31 <sup>56</sup>	-	-	0.90	-
Ni	943	111	5.35	5.34 <sup>56</sup>	-	-	2.02	2.34 <sup>70</sup>
Ag	813	001	4.5	4.2 <sup>56</sup>	-	-	0.99	-
Cu	867	001	4.7	5.1 <sup>56</sup>	-	-	1.47	-
Pd	963	111	5.54	5.6 <sup>56</sup>	-	-	1.57	-
Pt	972	001	5.97	5.93 <sup>56</sup>	-	-	1.94	-
Ti	1029	100	3.84	4.33 <sup>56</sup>	-	-	2.27	-
Mg	919	100	3.76	3.66 <sup>56</sup>	-	-	0.35	-
Na	931	001	2.97	2.36 <sup>56</sup>	-	-	0.10	-
Hf	802	111	3.7	3.9 <sup>56</sup>	-	-	2.02	-
Co	858	001	5.22	5.0 <sup>56</sup>	-	-	3.49	-
Rh	984	001	5.4	4.98 <sup>56</sup>	-	-	2.46	-
Ir	901	100	5.85	5.67 <sup>56</sup>	-	-	2.77	-
Nb	934	100	3.87	4.02 <sup>56</sup>	-	-	2.41	-
Re	981	100	4.96	4.72 <sup>56</sup>	-	-	2.87	-
Mo	21195	100	4.17	4.53 <sup>56</sup>	-	-	3.30	-
Zn	1056	001	4.27	4.24 <sup>71</sup>	-	-	0.36	-
Bi	837	001	4.31	4.34 <sup>56</sup>	-	-	0.65	0.43 <sup>72</sup>
Cr	861	110	5.04	4.5 <sup>56</sup>	-	-	3.31	-
Sb	993	001	4.64	4.7 <sup>56</sup>	-	-	0.67	-
Sn	1008	110	4.82	4.42 <sup>56</sup>	-	-	0.91	-
MAE	-	-	0.29	-	0.39	-	0.34	-

procedure mentioned above. In this way, we find precision scores of 55.0 %, 63.4 % and 60.0 % respectively suggesting that structure optimization of surfaces has an impact on the ALIGNN predictions. Still, sufficiently high precision scores suggest that such models can be used for pre-screening applications followed by density functional theory calculations and experiments. Also, as the DFT bulk, surface and interface dataset is growing continuously, there is plenty of scope to improve the model performance in the future. For the 1.4 trillion semiconductor interfaces, we find 294 billion as type-I, 322 billion as type-II and rest as type-III heterostructures using the ALIGNN+IU model. The results suggest that finding type-I interfaces for transistor



applications is more challenging than other heterostructure applications. Having such a large number of options and further screened for desirable properties such as effective masses, dielectric, piezoelectric, thermoelectric properties etc. can be helpful for technological applications. We emphasize the point that AI models should be considered as a pre-screening step only and would require thorough DFT and/or experimental validation.

### Interface geometry generation and alternate slab junction (ASJ) model

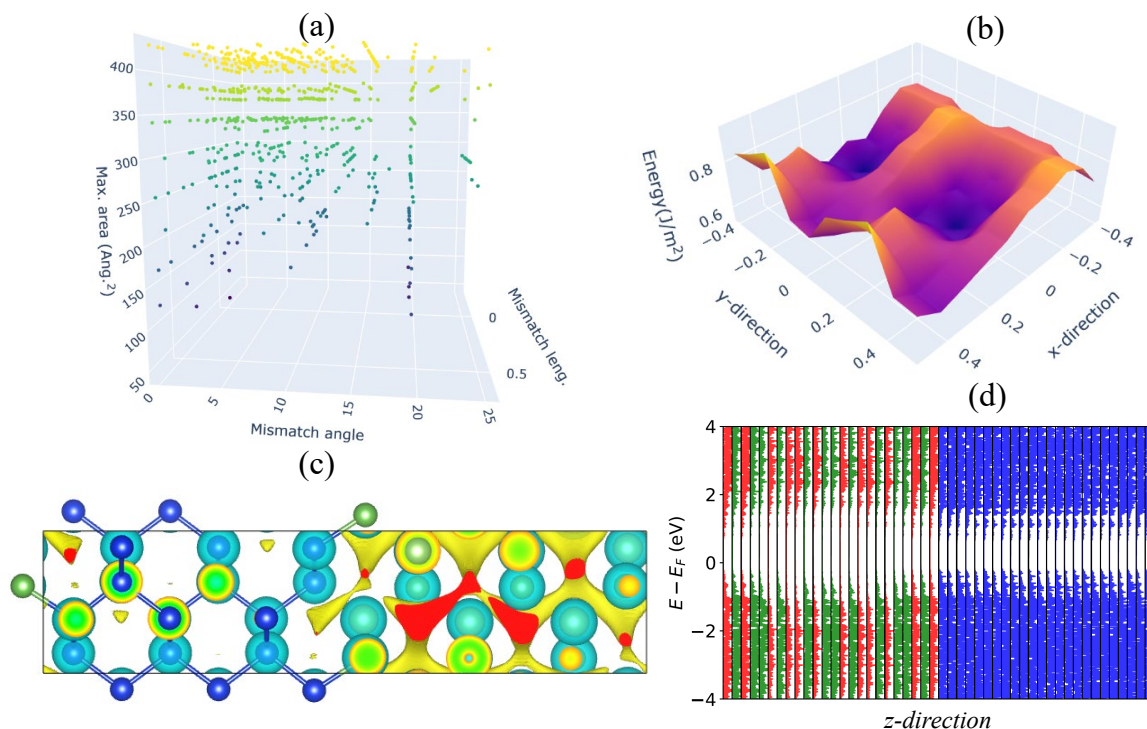


**Figure 4.** Structure generation criteria selection and initial xy-plane scan with ALIGNN-FF for Si(110)/GaAs(110) interface. a) All the parameters such as mismatch in x-direction ( $u$ ), mismatch in y-direction ( $v$ ) and maximum allowed are optimized to generate suitable structures. b) To save computational cost, a pre-screening of the optimum xy-plane scan is carried out using ALIGNN-FF and then subjected to computational method such as DFT. c) electrostatic potential of the system. d) atom projected density of states for the system, separated along the z direction. Red, green and blue colors represent gallium, arsenic and silicon atom contributions respectively.

To go beyond the limits of the IU model, we next consider explicit DFT calculations of interfaces, which first require generating candidate interface structures. This can be done in either of the following two ways: 1) by attaching the two surface slabs together without vacuum padding, which leads to superlattice or alternating slab junction (ASJ) models, or 2) by attaching the two surface slabs with vacuum padding, surface terminated junctions (SJT). Currently, we have interface properties calculated with the ASJ approach. We first obtain the bulk atomic structures as well as convergence data from JARVIS-DFT. We generate the interfaces following the Zur *et. al.* algorithm<sup>76</sup>. The Zur algorithm generates a number of superlattice transformations within a specified maximum surface area and also evaluates the length and angle between film and substrate superlattice vectors to determine if they can match within a tolerance. This algorithm is applicable to different crystal structures and their surface orientations. We use a maximum lattice mismatch of 8 %, maximum area of  $300 \text{ \AA}^2$ , and maximum angle tolerance of 1 degree. Note that in previous studies, lattice mismatch of 20 % has been reported<sup>11,77</sup>. An example of the application of the algorithm to the Si(110)/GaAs(110) interface is shown in Fig. 4a. After eliminating structures with area higher than max-area tolerance and structures with mismatch angle more than the specified angle threshold, we then choose the remaining structure (if any) with the minimum mismatch lattice vector lengths.

Thus far, we have determined a candidate unit cell, but the relative alignment of the structures in the in-plane, as well as the terminations still need to be decided. We perform a grid search of possible in-plane alignments with a space of 0.05 fractional coordinates to determine the initial structure for further relaxation. Doing such a large number of calculation with DFT would be prohibitive, so we use ALIGNN-FF<sup>74</sup> to identify the starting in-plane alignment. Additionally, ALIGNN-FF can be used

to pre-relax the structure as well. ALIGNN-FF is a universal force field ML model developed using JARVIS-DFT data with 307113 structures and can be used to model combinations of 89 elements from the periodic table. An example of ALIGNN-FF predictions of an in-plane grid serach is shown in Fig. 4b. Here high-peaks usually represent too close atoms during the translation operations, which should be avoided. After the ALIGNN-FF calculations, a full DFT relaxation is performed.

For computational purposes, it is important to have a unique identifier for an interface. While generating the interfaces, we use a naming convention to include a) material IDs (such as JVASP-1002 for Si and JVASP-1174 for GaAs), b) film and substrate Miller indices (such as 110 for each), c) film and substrate thickness values (such as 16 Å each), d) separation between these two surface slabs (such as 2.5 Å for an ASJ model, 18 Å for STJ interface models), e) relative displacement in xy-plane (such as a displacement vector of [0.5, 0.2]), f) calculator method (such as DFT (VASP), ALIGNN-FF etc.) giving rise to an interface with a name such as Interface-JVASP-1002\_JVASP-1174\_film\_miller\_1\_1\_0\_sub\_miller\_1\_1\_0\_film\_thickness\_16\_subs\_thickness\_16\_separation\_2.5\_0.2\_vasp. Such a scheme helps to reproduce the unique interfaces. Of course, realistically, more complex parameters for an interface can be important such as terminations, reconstructions, misfit-dislocation, vacancies on the interface etc., but they can be easily included in the naming scheme as well later.

After selecting a good guess of the interface using the above approach, DFT calculations are performed to calculate the band offset value. During the DFT calculations, maximum value of the two converged K-point and energy cutoff for constituent bulk materials<sup>73</sup> are used. An example of the Si(110) and GaAs(110) interface along with its DFT electrostatic potential is shown in Fig. 4c. Furthermore, we can project the electron density of states across the cell dimension in Fig.4d to show how electronic states are distributed along the interface region. Clearly, at the interface region, the GaAs band gap decreases due to the Si part. Such analysis can also help understand the band alignment but from the atomic contribution of electronic states perspective and over the length-scale of the device.

After determining the optimized geometric structure for the interface using DFT, we obtain band offset data using formalism detailed in Ref.<sup>8</sup>. As an example, we show a detailed analysis of Si(110)/GaAs(110) and AlN(001)/GaN(001) in Fig. 5. In Fig. 5a, we show the atomic structure of the ASJ based heterostructure of Si(110)/GaAs(110). The left side (with blue atoms) represents the Si and the right side is the GaAs region. In Fig. 5c, we show the electrostatic potential profile, averaged in-plane, of the interface. The approximately sinusoidal profile on both regions represents the presence of atomic layers. The cyan lines show the region used to define the repeat distance,  $L$ , used for averaging in each material (see below). The red and green lines show the average potential profiles for the left and right parts using the repeat distance. The valence band offset ( $\Delta E_v$ ) of an interface between semiconductor A and B,  $\Delta E_v$  is obtained using eq. 4. The difference in the averages for the left and right parts gives the  $\Delta V$  term. Now the bulk VBMs of the left and right parts are also calculated to determine the  $\Delta E$ . The sum of these two quantities gives the band offset that can be compared to experiments.

$$\Delta E_v(A/B) = (E_v^B - E_v^A) + \Delta V \quad (4)$$

$$\Delta V = \bar{V}_A - \bar{V}_B \quad (5)$$

Here,  $E_v^A$  ( $E_v^B$ ) represents the position of the VBM with respect to the average electrostatic potential in the bulk material A (B), and  $\Delta V$  represents dipole potential or the difference between the macroscopic-averaged electrostatic potential between A and B. Moreover,  $\bar{V}$  is the average along the repeat unit  $L$  of  $\bar{V}$ , which is the planar averaged electrostatic potential:

$$\bar{V}(z) = \frac{1}{L} \int_{-L/2}^{L/2} \bar{V}(z+z') dz' \quad (6)$$

$\bar{V}$  is given by:

$$\bar{V}(z) = \frac{1}{S} \int_S V(x,y,z) dx dy \quad (7)$$

where,  $L$  is the distance between repeat units and  $S$  is the area which is parallel to the interface. The corresponding conduction-band offset can be determined by using band-gap values from the respective bulk calculations, or experimental data. We will use the convention that a positive value of the valence-band offset at an interface A/B indicates that the VBM is higher in material B. For the GaAs/Si interface we obtain  $\Delta E_v$  of 0.31 eV and 0.39 eV using OptB88vdW and R2SCAN functionals, respectively, which is in close agreement with the experimental value of 0.23 eV.



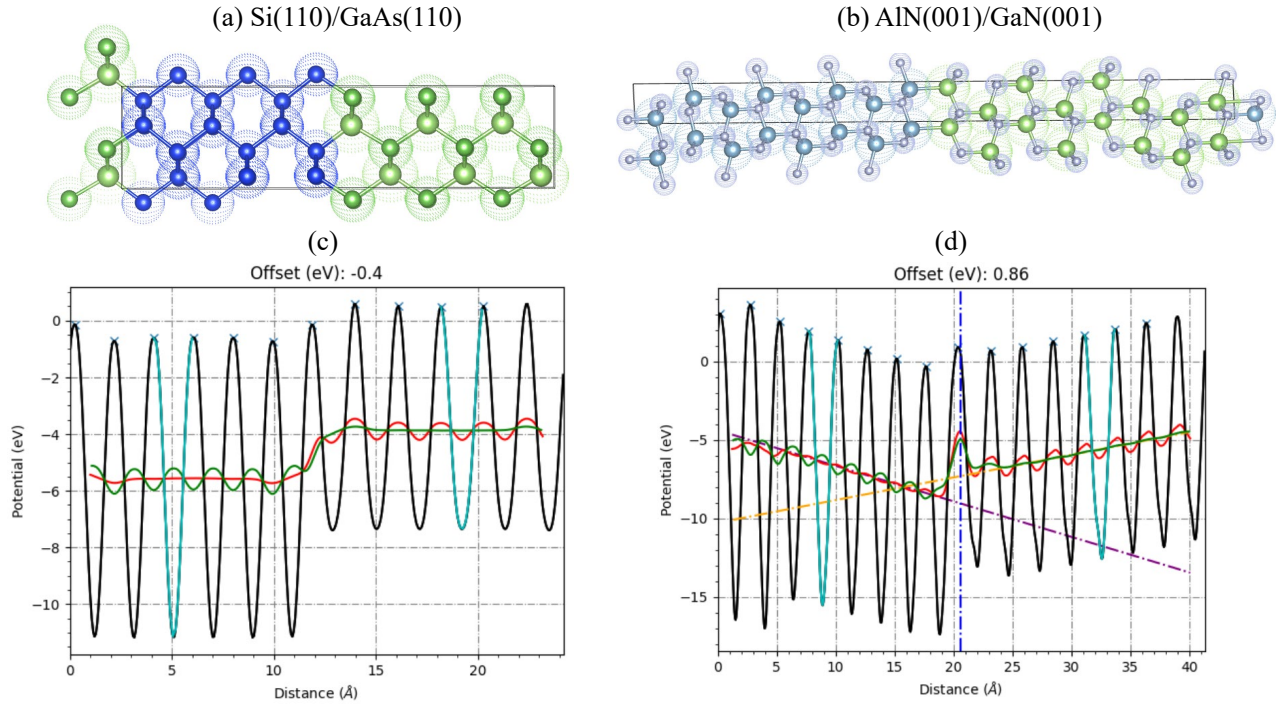


**Figure 5.** Atomic structures and band-alignment using the average electrostatic potential of metal-semiconductor and semiconductor-semiconductor interfaces. a) atomic structure view of Si/GaAs(110), b) atomic structure view of polar interface AlN/GaN(001), c) electrostatic potential profile for Si/GaAs(110), d) average electrostatic potential profile for polar surfaces of AlN/GaN (001). The cyan lines are used to find the repeat unit layers for the left and right parts. The linear parts of the red and green lines show the average potential profiles for the left and right parts using the repeat distance mentioned above. The dotted vertical blue line denotes the interface.

Next, we show a polar semiconductor heterojunction example for AlN (001)/GaN(001) interface in Fig. 5b. The electrostatic potential profile is shown in Fig. 5d. In contrast to flat average potential values in Fig. 5c, we observe inclined profiles for this system representing indicating the presence of a constant electric field. We fit lines for both sides and extrapolate to the interface. The difference of the lines at the interface gives  $\Delta V$ . The calculation of  $\Delta E$  remains the same as the non-polar case. These calculations are automated in the workflow, however, it is important to check that the slab is thick enough to define a bulk-like region where  $\bar{V}(z)$  is linear. Now, in the Table. 2 we compare some of the ASJ based valence band offsets ( $\Delta E_v$ ) with experimental measurements. We find a mean absolute error of 0.22 eV and 0.23 eV for OptB88vdW and R2SCAN respectively, which is comparable a value of 0.16 eV from to Liberto *et. al.* for a smaller number of systems using the HSE06 functional. In future, we plan to carry out HSE06 calculations for surfaces as well as interfaces to further improve the quality of predictions. These benchmarks will also be available in the JARVIS-Leaderboard platform<sup>97</sup> as well. Out of numerous possible combinations, only 250 DFT calculations of ASJ-based interfaces are available right now and the database is still growing.

In summary, we have provided a computational framework and dataset for investigating interface systems using multi-fidelity computational approaches. We have developed one of the largest datasets, containing 300 surfaces, 44850 IU-band offsets, and 250 ASJ interface band offset using DFT. Using universal graph neural network models, we have quickly screened potential semiconductor device candidates as transistors from a pool of 1.4 trillion possible interfaces, which would not have been possible using conventional computational or experimental techniques. Although we have applied this framework for semiconductors, it can be useful for other technological applications as well. After pre-screening, we have shown and benchmarked this streamlined workflow for band offset predictions using independent unit and alternate slab junction models. This work paves the way for the application of materials design approach to interface systems. All of the tools and datasets developed in this work will be distributed publicly in the spirit of open-science.

**Table 2.** Band offsets (in eV) of a few independent unit (IU)/Anderson’s model and alternating slab-junction (ASJ) based semiconductor/semiconductor interfaces with OptB88vdW (OPT) and R2SCAN functionals in comparison to previously reported experiments. Here ID, Miller and P represent a JARVIS-DFT identifier, Miller index and polar surface interfaces respectively.

System	ID	Miller	IU (OPT)	ASJ (OPT)	ASJ (R2SCAN)	Exp
AlP/Si	1327/1002	110/110	1.24	0.88	1.04	1.35 <sup>13</sup>
GaAs/Si	1174/1002	110/110	0.30	0.31	0.39	0.23 <sup>78</sup>
CdS/Si	8003/1002	110/110	3.22	1.48	1.70	1.6 <sup>79</sup>
AlAs/GaAs	1372/1174	110/110	0.60	0.48	0.50	0.55 <sup>80</sup>
CdS/CdSe	8003/1192	110/110	0.35	0.10	0.11	0.55 <sup>81</sup>
InP/GaAs	1183/1174	110/110	0.25	0.72	0.75	0.19 <sup>82</sup>
ZnTe/AlSb	1198/1408	110/110	0.8	0.25	0.33	0.35 <sup>83</sup>
CdSe/ZnTe	1192/1198	110/110	1.8	0.58	0.67	0.64 <sup>84</sup>
InAs/AlAs	1186/1372	110/110	-	0.46	0.39	0.5 <sup>85</sup>
InAs/AlSb	1186/1408	110/110	-	0.05	0.16	0.09 <sup>86</sup>
ZnSe/InP	96/1183	110/110	-	0.13	0.18	0.41 <sup>87</sup>
InAs/InP	1186/1183	110/110	-	0.11	0.09	0.31 <sup>82</sup>
ZnSe/AlAs	96/1372	110/110	-	0.38	0.45	0.4 <sup>88</sup>
GaAs/ZnSe	1174/96	110/110	-	0.72	0.80	0.98 <sup>89</sup>
ZnS/Si	10591/1002	001/001	-	0.92	1.16	1.52 <sup>90</sup>
Si/SiC	1002/8118	001/001	-	0.51	0.47	0.5 <sup>91</sup>
GaN/SiC (P)	30/8118	001/001	-	1.12	1.37	0.70 <sup>92</sup>
Si/AlN (P)	1002/30	001/001	-	3.51	3.60	3.5 <sup>93</sup>
GaN/AlN (P)	30/39	001/001	-	0.80	0.86	0.73 <sup>94</sup>
AlN/InN (P)	39/1180	001/001	-	1.24	1.07	1.81 <sup>95</sup>
GaN/ZnO (P)	30/1195	001/001	-	0.51	0.46	0.7 <sup>96</sup>
MAE	-	-	0.45	0.22	0.23	-

## Methods

Graph neural networks are trained using Atomistic Line Graph Neural Network (ALIGNN) framework<sup>49</sup> which uses PyTorch and deep graph library (DGL). ALIGNN is trained for 500 epochs and with default parameters in the package. We use a 90:5:5 training:validation:testing data split for the CBM and VBM for the bulk materials dataset. DFT calculations were carried out using the Vienna Ab-initio simulation package (VASP) software<sup>98,99</sup> with OptB88vdW<sup>41</sup>, TBmBJ<sup>42</sup> and R2SCAN<sup>43</sup> functionals using the workflow given on our ‘jarvis-tools’ GitHub page (<https://github.com/usnistgov/jarvis>). Please note commercial software is identified to specify procedures. Such identification does not imply recommendation by National Institute of Standards and Technology (NIST). We use the OptB88vdW functional, which gives accurate lattice parameters for both vdW and non-vdW (3D-bulk) solids. The crystal structure was optimized until the forces on the ions were less than 0.01 eV/Å and energy less than 10<sup>-6</sup> eV. Also, we calculate the local potential containing ionic plus Hartree contributions to determine the vacuum potential (VAC) of surface slabs. The VAC is subtracted from the valence band maxima (VBM) and conduction band minima (CBM) to enable the comparison of band-diagrams of individual slabs in band-alignment diagrams. The converged k-points and cut-off for the bulk materials were also used for the corresponding surface slab models. The ASJ based interface structures were generated using Zur algorithm<sup>76</sup> available in the JARVIS-Tools. For a quick scan of xy-displacements for surfaces in the interfaces, ALIGNN-FF was used.

## Acknowledgements

We thank computational resource from National Institute of Standards and Technology (NIST).

## Author contributions statement

K.C. conceived the high-throughput workflow and conducted all calculations, K.F.G helped in setting up calculations and analysing the results. All authors reviewed the manuscript.

## Competing interests

The authors declare no competing interests.

## Data availability

The data generated by this work will be made publicly available at Figshare and JAVRIS website (<https://jarvis.nist.gov/jarvish/>).

## Code availability

The code used in this work, InterMat will be made publicly available at : <https://github.com/usnistgov/intermat>. It depends on closely related codes available at <https://github.com/usnistgov/jarvis> and <https://github.com/usnistgov/alignn>.

## References

1. Kroemer, H. Heterostructure bipolar transistors and integrated circuits. *Proc. IEEE* **70**, 13–25 (1982).
2. Mönch, W. *Electronic properties of semiconductor interfaces*, vol. 43 (Springer Science & Business Media, 2013).
3. Edward, T. Y., McCaldin, J. O. & McGill, T. C. Band offsets in semiconductor heterojunctions. In *Solid state physics*, vol. 46, 1–146 (Elsevier, 1992).
4. Robertson, J. Band offsets, schottky barrier heights, and their effects on electronic devices. *J. Vac. Sci. & Technol. A* **31** (2013).
5. Smeu, M. & Leung, K. Electron leakage through heterogeneous lif on lithium–metal battery anodes. *Phys. Chem. Chem. Phys.* **23**, 3214–3218 (2021).
6. Agostini, G. & Lamberti, C. *Characterization of semiconductor heterostructures and nanostructures* (Elsevier, 2011).
7. Taur, Y. The incredible shrinking transistor. *Ieee Spectr.* **36**, 25–29 (1999).
8. Van de Walle, C. G. & Martin, R. M. Theoretical study of si/ge interfaces. *J. Vac. Sci. & Technol. B: Microelectron. Process. Phenom.* **3**, 1256–1259 (1985).
9. Franciosi, A. & Van de Walle, C. G. Heterojunction band offset engineering. *Surf. Sci. Reports* **25**, 1–140 (1996).
10. Weston, L., Taylor, H., Krishnaswamy, K., Bjaalie, L. & Van de Walle, C. Accurate and efficient band-offset calculations from density functional theory. *Comput. Mater. Sci.* **151**, 174–180 (2018).
11. Hinuma, Y., Grüneis, A., Kresse, G. & Oba, F. Band alignment of semiconductors from density-functional theory and many-body perturbation theory. *Phys. Rev. B* **90**, 155405 (2014).
12. Ghosh, A. *et al.* Efficient and improved prediction of the band offsets at semiconductor heterojunctions from meta-gga density functionals: A benchmark study. *The J. Chem. Phys.* **157** (2022).
13. Di Liberto, G. & Pacchioni, G. Band offset in semiconductor heterojunctions. *J. Physics: Condens. Matter* **33**, 415002 (2021).
14. Dardzinski, D., Yu, M., Moayedpour, S. & Marom, N. Best practices for first-principles simulations of epitaxial inorganic interfaces. *J. Physics: Condens. Matter* **34**, 233002 (2022).
15. Mathew, K. *et al.* Mpinterfaces: A materials project based python tool for high-throughput computational screening of interfacial systems. *Comput. Mater. Sci.* **122**, 183–190 (2016).
16. Choudhary, K., Garrity, K. F., Hartman, S. T., Pilania, G. & Tavazza, F. Efficient computational design of two-dimensional van der waals heterostructures: Band alignment, lattice mismatch, and machine learning. *Phys. Rev. Mater.* **7**, 014009 (2023).
17. Restuccia, P., Losi, G., Chehaimi, O., Marsili, M. & Righi, M. C. High-throughput first-principles prediction of interfacial adhesion energies in metal-on-metal contacts. *ACS Appl. Mater. & Interfaces* **15**, 19624–19633 (2023).
18. Choudhary, K., Liang, T., Chernatynskiy, A., Phillpot, S. R. & Sinnott, S. B. Charge optimized many-body (comb) potential for al<sub>2</sub>o<sub>3</sub> materials, interfaces, and nanostructures. *J. Physics: Condens. Matter* **27**, 305004 (2015).
19. Yu, J., Sinnott, S. B. & Phillpot, S. R. Charge optimized many-body potential for the si/ sio<sub>2</sub> system. *Phys. Rev. B* **75**, 085311 (2007).

20. Shan, T.-R. *et al.* Charge-optimized many-body potential for the hafnium/hafnium oxide system. *Phys. Rev. B* **81**, 125328 (2010).
21. Hahn, K. R., Puligheddu, M. & Colombo, L. Thermal boundary resistance at si/ge interfaces determined by approach-to-equilibrium molecular dynamics simulations. *Phys. Rev. B* **91**, 195313 (2015).
22. Harrison, W. & Tersoff, J. Tight-binding theory of heterojunction band lineups and interface dipoles. *J. Vac. Sci. & Technol. B: Microelectron. Process. Phenom.* **4**, 1068–1073 (1986).
23. Bernstein, N., Aziz, M. J. & Kaxiras, E. Amorphous-crystal interface in silicon: A tight-binding simulation. *Phys. Rev. B* **58**, 4579 (1998).
24. Schenter, G. K. & LaFemina, J. P. Semiconductor surface and interface dynamics from tight-binding molecular dynamics simulations. *J. Vac. Sci. & Technol. A: Vacuum, Surfaces, Films* **10**, 2429–2435 (1992).
25. Munoz, M., Velasco, V. & Garcia-Moliner, F. Tight binding models for non ideal semiconductor interfaces. *Prog. surface science* **26**, 117–133 (1987).
26. Willhelm, D. *et al.* Predicting van der waals heterostructures by a combined machine learning and density functional theory approach. *ACS Appl. Mater. & Interfaces* **14**, 25907–25919 (2022).
27. Huang, Y. *et al.* Band gap and band alignment prediction of nitride-based semiconductors using machine learning. *J. Mater. Chem. C* **7**, 3238–3245 (2019).
28. Zhu, Z., Dong, B., Guo, H., Yang, T. & Zhang, Z. Fundamental band gap and alignment of two-dimensional semiconductors explored by machine learning. *Chin. Phys. B* **29**, 046101 (2020).
29. Milnes, A. G. *Heterojunctions and metal semiconductor junctions* (Elsevier, 2012).
30. Robertson, J. High dielectric constant gate oxides for metal oxide si transistors. *Reports on progress Phys.* **69**, 327 (2005).
31. Roul, B., Kumar, M., Rajpalke, M. K., Bhat, T. N. & Krupanidhi, S. Binary group iii-nitride based heterostructures: band offsets and transport properties. *J. Phys. D: Appl. Phys.* **48**, 423001 (2015).
32. Ohler, C., Daniels, C., Förster, A. & Lüth, H. Heterojunction band offsets and schottky-barrier heights: Tersoff's theory in the presence of strain. *Phys. Rev. B* **58**, 7864 (1998).
33. Schottky, W. Small-shot effect and flicker effect. *Phys. Rev.* **28**, 74 (1926).
34. Bardeen, J. Surface states and rectification at a metal semi-conductor contact. *Phys. review* **71**, 717 (1947).
35. Oliveira, L. N. & Wilkins, J. W. Fano antiresonances in x-ray-absorption spectroscopy. *Phys. Rev. B* **32**, 696 (1985).
36. Anderson, R. Germanium-gallium arsenide heterojunctions. *IBM J. Res. Dev.* **4**, 283–287 (1960).
37. Losi, G., Chehaimi, O. & Righi, M. C. Tribchem: a software for the first-principles, high-throughput study of solid interfaces and their tribological properties. *arXiv preprint arXiv:2304.14367* (2023).
38. Smidstrup, S. *et al.* Quantumatk: An integrated platform of electronic and atomic-scale modelling tools. *J. Physics: Condens. Matter* **32**, 015901 (2019).
39. Wines, D. *et al.* Recent progress in the JARVIS infrastructure for next-generation data-driven materials design. *Appl. Phys. Rev.* **10**, 041302 (2023).
40. Choudhary, K. *et al.* The joint automated repository for various integrated simulations (jarvis) for data-driven materials design. *npj computational materials* **6**, 173 (2020).
41. Klimeš, J., Bowler, D. R. & Michaelides, A. Chemical accuracy for the van der waals density functional. *J. Physics: Condens. Matter* **22**, 022201 (2009).
42. Tran, F. & Blaha, P. Accurate band gaps of semiconductors and insulators with a semilocal exchange-correlation potential. *Phys. review letters* **102**, 226401 (2009).
43. Furness, J. W., Kaplan, A. D., Ning, J., Perdew, J. P. & Sun, J. Accurate and numerically efficient r2scan meta-generalized gradient approximation. *The journal physical chemistry letters* **11**, 8208–8215 (2020).
44. Heyd, J., Scuseria, G. E. & Ernzerhof, M. Hybrid functionals based on a screened coulomb potential. *The J. chemical physics* **118**, 8207–8215 (2003).
45. Choudhary, K. & Garrity, K. Designing high-*tc* superconductors with bcs-inspired screening, density functional theory, and deep-learning. *npj Comput. Mater.* **8**, 244 (2022).

46. Wines, D., Choudhary, K., Biacchi, A. J., Garrity, K. F. & Tavazza, F. High-throughput dft-based discovery of next generation two-dimensional (2d) superconductors. *Nano letters* **23**, 969–978 (2023).
47. Choudhary, K. *et al.* Recent advances and applications of deep learning methods in materials science. *npj Comput. Mater.* **8**, 59 (2022).
48. Vasudevan, R. K. *et al.* Materials science in the artificial intelligence age: high-throughput library generation, machine learning, and a pathway from correlations to the underpinning physics. *MRS communications* **9**, 821–838 (2019).
49. Choudhary, K. & DeCost, B. Atomistic line graph neural network for improved materials property predictions. *npj Comput. Mater.* **7**, 185 (2021).
50. Choudhary, K., Gurunathan, R., DeCost, B. & Biacchi, A. Atomvision: A machine vision library for atomistic images. *J. Chem. Inf. Model.* **63**, 1708–1722 (2023).
51. Choudhary, K. & Kelley, M. L. Chemnlp: A natural language-processing-based library for materials chemistry text data. *The J. Phys. Chem. C* **127**, 17545–17555 (2023).
52. Dillon Jr, J. & Farnsworth, H. Work function and sorption properties of silicon crystals. *J. Appl. Phys.* **29**, 1195–1202 (1958).
53. Bhattacharya, P. *Semiconductor optoelectronic devices* (Prentice-Hall, Inc., 1997).
54. Messmer, C. & Bilello, J. The surface energy of si, gaas, and gap. *J. Appl. Phys.* **52**, 4623–4629 (1981).
55. Jaccodine, R. Surface energy of germanium and silicon. *J. electrochemical society* **110**, 524 (1963).
56. Hölzl, J. & Schulte, F. K. Work function of metals. *Solid surface physics* 1–150 (2006).
57. Field, J. & Freeman, C. Strength and fracture properties of diamond. *Philos. Mag. A* **43**, 595–618 (1981).
58. Gobeli, G. & Allen, F. Photoelectric properties and work function of cleaved germanium surfaces. *Surf. Sci.* **2**, 402–408 (1964).
59. Pouch, S. *et al.* Work function measurement of silicon germanium heterostructures combining kelvin force microscopy and x-ray photoelectron emission microscopy. *The J. Phys. Chem. C* **119**, 26776–26782 (2015).
60. Pelletier, J., Gervais, D. & Pomot, C. Application of wide-gap semiconductors to surface ionization: work functions of aln and sic single crystals. *J. applied physics* **55**, 994–1002 (1984).
61. Liu, W., Zheng, W. & Jiang, Q. First-principles study of the surface energy and work function of iii-v semiconductor compounds. *Phys. Rev. B* **75**, 235322 (2007).
62. Wu, C., Kahn, A., Hellman, E. & Buchanan, D. Electron affinity at aluminum nitride surfaces. *Appl. physics letters* **73**, 1346–1348 (1998).
63. Rosa, A. & Neugebauer, J. First-principles calculations of the structural and electronic properties of clean gan (0001) surfaces. *Phys. Rev. B* **73**, 205346 (2006).
64. Lin, S.-C. *et al.* Experimental determination of electron affinities for inn and gan polar surfaces. *Appl. physics express* **5**, 031003 (2012).
65. Lu, S. *et al.* Towards n-type conductivity in hexagonal boron nitride. *Nat. Commun.* **13**, 3109 (2022).
66. Crovetto, A. *et al.* Boron phosphide films by reactive sputtering: Searching for a p-type transparent conductor. *Adv. Mater. Interfaces* **9**, 2200031 (2022).
67. Csik, I., Russo, S. P. & Mulvaney, P. Density functional study of non-polar surfaces of wurtzite cdse. *Chem. physics letters* **414**, 322–325 (2005).
68. Haase, M., Cheng, H., DePuydt, J. & Potts, J. Characterization of p-type znse. *J. applied physics* **67**, 448–452 (1990).
69. Shen, K. *et al.* Insights into the role of interface modification in performance enhancement of znse: Cu contacted cdte thin film solar cells. *Sol. Energy* **201**, 55–62 (2020).
70. Clark, E., Yeske, R. & Birnbaum, H. The effect of hydrogen on the surface energy of nickel. *Metall. Transactions A* **11**, 1903–1908 (1980).
71. Ashcroft, N. W. & Mermin, N. D. *Solid state physics* (Cengage Learning, 2022).
72. Tran, R. *et al.* Surface energies of elemental crystals. *Sci. data* **3**, 1–13 (2016).
73. Choudhary, K. & Tavazza, F. Convergence and machine learning predictions of monkhorst-pack k-points and plane-wave cut-off in high-throughput dft calculations. *Comput. materials science* **161**, 300–308 (2019).



74. Choudhary, K. *et al.* Unified graph neural network force-field for the periodic table: solid state applications. *Digit. Discov.* **2**, 346–355 (2023).
75. Choudhary, K. & Sumpter, B. G. Can a deep-learning model make fast predictions of vacancy formation in diverse materials? *AIP Adv.* **13** (2023).
76. Zur, A. & McGill, T. Lattice match: An application to heteroepitaxy. *J. applied physics* **55**, 378–386 (1984).
77. Goodhew, P. & Giannakopoulos, K. Strain relaxation in iii–v semiconductor heterostructures. *Micron* **30**, 59–64 (1999).
78. List, R., Woicik, J., Lindau, I. & Spicer, W. The si/gaas (110) heterojunction: Strain, disorder, and valence-band discontinuity. *J. Vac. Sci. & Technol. B: Microelectron. Process. Phenom.* **5**, 1279–1283 (1987).
79. Kundu, M., Mahamuni, S., Gokhale, S. & Kulkarni, S. Chemical reactivity and band offset at the cds/si interface. *Appl. surface science* **68**, 95–102 (1993).
80. Batey, J. & Wright, S. Energy band alignment in gaas:(al, ga) as heterostructures: The dependence on alloy composition. *J. Appl. Phys.* **59**, 200–209 (1986).
81. Talapin, D. V. *et al.* Highly emissive colloidal cdse/cds heterostructures of mixed dimensionality. *Nano Lett.* **3**, 1677–1681 (2003).
82. Waldrop, J., Grant, R. & Kraut, E. Measurement of gaas/inp and inas/inp heterojunction band offsets by x-ray photoemission spectroscopy. *Appl. physics letters* **54**, 1878–1880 (1989).
83. Schwartz, G., Gualtieri, G., Feldman, R., Austin, R. & Nuzzo, R. Band offset measurements for alsb/znte heterojunctions. *J. Vac. Sci. & Technol. B: Microelectron. Process. Phenom.* **8**, 747–750 (1990).
84. Yu, E., Phillips, M., McCaldin, J. & McGill, T. Measurement of the cdse/znte valence band offset by x-ray photoelectron spectroscopy. *J. Vac. Sci. & Technol. B: Microelectron. Nanometer Struct. Process. Meas. Phenom.* **9**, 2233–2237 (1991).
85. Arriaga, J. *et al.* Electronic structure of strained-layer alas/inas (001) superlattices. *Phys. Rev. B* **43**, 2050 (1991).
86. Nakagawa, A., Kroemer, H. & English, J. H. Electrical properties and band offsets of inas/alsb n-n isotype heterojunctions grown on gaas. *Appl. physics letters* **54**, 1893–1895 (1989).
87. Lange, H. & Kelley, D. F. Spectroscopic effects of lattice strain in inp/znse and inp/zns nanocrystals. *The J. Phys. Chem. C* **124**, 22839–22844 (2020).
88. Rubini, S., Milocco, E., Sorba, L. & Franciosi, A. Transitivity of the band offsets in ii–vi/iii–v heterojunctions. *J. crystal growth* **184**, 178–182 (1998).
89. Kowalczyk, S. P., Kraut, E., Waldrop, J. & Grant, R. Measurement of znse–gaas (110) and znse–ge (110) heterojunction band discontinuities by x-ray photoelectron spectroscopy (xps). *J. Vac. Sci. Technol.* **21**, 482–485 (1982).
90. Lew Yan Voon, L., Ram-Mohan, L. & Soref, R. Electronic and optical properties of (001) si/zns heterostructures. *Appl. physics letters* **70**, 1837–1839 (1997).
91. Dufour, G. *et al.* Sic formation by reaction of si (001) with acetylene: Electronic structure and growth mode. *Phys. Rev. B* **56**, 4266 (1997).
92. Rizzi, A. *et al.* Aln and gan epitaxial heterojunctions on 6h–sic (0001): Valence band offsets and polarization fields. *J. Vac. Sci. & Technol. B: Microelectron. Nanometer Struct. Process. Meas. Phenom.* **17**, 1674–1681 (1999).
93. King, S. W., Nemanich, R. J. & Davis, R. F. Band alignment at aln/si (111) and (001) interfaces. *J. Appl. Phys.* **118** (2015).
94. Sang, L. *et al.* Band offsets of non-polar a-plane gan/aln and aln/gan heterostructures measured by x-ray photoemission spectroscopy. *Nanoscale Res. Lett.* **9**, 1–5 (2014).
95. Waldrop, J. & Grant, R. Measurement of aln/gan (0001) heterojunction band offsets by x-ray photoemission spectroscopy. *Appl. physics letters* **68**, 2879–2881 (1996).
96. Liu, J. *et al.* Band offsets of polar and nonpolar gan/zno heterostructures determined by synchrotron radiation photoemission spectroscopy. *physica status solidi (b)* **248**, 956–959 (2011).
97. Choudhary, K. *et al.* Large scale benchmark of materials design methods. *arXiv preprint arXiv:2306.11688* (2023).
98. Kresse, G. & Furthmüller, J. Efficient iterative schemes for ab initio total-energy calculations using a plane-wave basis set. *Phys. review B* **54**, 11169 (1996).
99. Kresse, G. & Furthmüller, J. Efficiency of ab-initio total energy calculations for metals and semiconductors using a plane-wave basis set. *Comput. materials science* **6**, 15–50 (1996).